JGR Solid Earth

Rapid Source Characterization of the Maule Earthquake Using Prompt Elasto-Gravity Signals

G. Arias[1] , Q. Bletery[1] , A. Licciardi[1] , K. Juhel[1,2] , J. P. Ampuero[1] , and B. Rouet-Leduc[3]

[1]Université Côte d'Azur, IRD, CNRS, Observatoire de la Côte d'Azur, Géoazur, Sophia Antipolis, Nice, France, [2]Laboratoire de Planétologie et Géosciences - UMR 6112, Université de Nantes, CNRS, Nantes, France, [3]Disaster Prevention Research Institute, Kyoto University, Kyoto, Japan

Abstract The recently identified Prompt Elasto-Gravity Signals (PEGS), generated by large earthquakes, propagate at the speed of light and are sensitive to the earthquake magnitude and focal mechanism. These characteristics make PEGS potentially very advantageous for tsunami early warning, which relies on fast and accurate estimation of the magnitude of large offshore earthquakes. PEGS-based early warning does not suffer from the problem of magnitude estimation saturation, that P-wave based early warning algorithms have, and could be faster than Global Navigation Satellite Systems (GNSS)-based systems while not requiring a priori assumptions on slip distribution. We use a deep learning model called PEGSNet to evaluate the possibility to estimate in real time the evolution of the magnitude of big earthquakes in the tsunamigenic zone of Chile. The model is a Convolutional Neural Network (CNN) trained on a database of synthetic PEGS—simulated for an exhaustive set of possible earthquakes distributed along the Chilean subduction zone—augmented with empirical noise. The approach is multi-station and leverages the information recorded by the seismic network to estimate as fast as possible the magnitude and location of an ongoing earthquake. Our results indicate that PEGSNet could have estimated that the magnitude of the 2010 M_w 8.8 Maule earthquake was above 8.7, 90 s after origin time. Our offline simulations using real data and noise recordings further support the instantaneous tracking of the source time function of the earthquake and show that deploying seismic stations in optimal locations could improve the performance of the algorithm.

Plain Language Summary Tsunami early warning requires the fast and reliable estimation of an earthquake magnitude provided by Earthquake Early Warning (EEW) systems. EEW systems are currently limited by the propagation speed of P-waves, which rely on as natural information carriers. Even more problematic, EEW systems based on the first seismic arrivals tend to saturate with earthquake magnitude, and can become unreliable for magnitudes above 8. The recent discovery of Prompt Elasto-Gravity Signals (PEGS), which comprise gravitational changes generated by earthquakes, has raised hope to overcome these limitations because they travel at the speed of light, much faster than P-waves. We use PEGS to re-train the previously developed deep learning model PEGSNet to track the magnitude evolution of big earthquakes in the Chilean subduction zone, historically affected by tsunamis. Given the scarcity of big earthquakes, we simulate signals to train the model using synthetic sources and the seismic stations available in 2010 and 2021, augmented with empirical noise recorded by those stations. PEGSNet tracks the moment release 90 s after the origin time. The performance of PEGSNet is limited by the seismic network configuration, the number of stations and the level of noise in the data, but could be useful for tsunami warning.

1. Introduction

Earthquakes redistribute Earth's mass, which produces changes in the gravitational field that lead to Prompt Elasto-Gravity Signals (PEGS) (Harms, 2016; Harms et al., 2015; Heaton, 2017; Montagner et al., 2016; Vallée et al., 2017). These signals precede conventional seismic waves and their amplitude depends on the earthquake source parameters, such as magnitude or focal mechanism (Juhel et al., 2019; Vallée & Juhel, 2019; Vallée et al., 2017; Zhang et al., 2020). These characteristics underlie the impact of their discovery and eventually their potential contribution to tsunami early warning (Allen & Melgar, 2019; Juhel et al., 2018; Licciardi et al., 2022; Shimoda et al., 2021; Zhang et al., 2022), since forecasting tsunami waves relies on the rapid estimation of earthquake magnitude (Melgar & Bock, 2013; Melgar et al., 2016; Setiyono et al., 2017) provided by Earthquake Early Warning (EEW) systems.

Conventional EEW systems have several limitations in estimating the final magnitude of an earthquake. Many EEW systems are designed to work with the first seconds of P-waves to forecast quickly the magnitude and source information once an earthquake occurred (Allen & Kanamori, 2003; Wu & Zhao, 2006), but the onset does not contain enough information to predict how large an earthquake is going to be (Meier et al., 2016). Additionally, EEW algorithms use the data of accelerometers that record the low-frequency content with low fidelity (Boore & Bommer, 2005; C. Ruhl et al., 2017). Overcoming these limitations is essential to prevent the underestimation of earthquake magnitude and impending hazards. For instance, during the 2011 Tohoku-Oki, Japan earthquake (M_w 9.0), the magnitude was estimated as M_w 8.1 at 116.8 s after the origin time (Hoshiba et al., 2011), which caused an underestimation of the subsequent tsunami amplitude (Hoshiba & Ozaki, 2014). Global Navigation Satellite Systems (GNSS) have been leveraged to overcome the drawbacks of earthquake and tsunami early warning (Bock & Melgar, 2016). GNSS-based algorithms can potentially solve the magnitude underestimation problem (Minson et al., 2014; C. Ruhl et al., 2017) but still use information (co-seismic ground deformation) traveling at the speed of P-waves (McGuire et al., 2021; Minson et al., 2018). GNSS-based algorithms that can accurately estimate the final rupture size also require the use of a priori constraints and inversion regularization that may be unpractical in real-time scenarios (McGuire et al., 2021).

PEGS present the fundamental property to propagate faster than seismic waves. In detail, they are the result of a direct gravity perturbation and an induced elastic response. The direct contribution consists of gravity perturbations ($\Delta \mathbf{g}$) caused by transient volumetric deformation and propagates at the speed of light; they arrive everywhere before any seismic wave. These gravity perturbations simultaneously act as secondary sources of elastic deformation in the whole Earth, inducing slight ground acceleration ($\ddot{\mathbf{u}}$). Due to the virtually instantaneous effect of the direct gravity perturbation, the induced ground acceleration also arrives before P-waves. The PEGS recorded by seismometers (acceleration $\mathbf{a}$) prior to the direct seismic wave arrival, is the sum of the direct gravity perturbation and the induced ground acceleration (Vallée et al., 2017):

$$\mathbf{a} = \Delta \mathbf{g} + \ddot{\mathbf{u}}. \tag{1}$$

In practice, $\Delta \mathbf{g}$ and $\ddot{\mathbf{u}}$ have opposite directions and similar magnitude, weakening the signal $\mathbf{a}$ (Heaton, 2017; Vallée et al., 2017).

The amplitudes of PEGS grow with the magnitude of the earthquake and depends on how fast the seismic moment rises (Vallée & Juhel, 2019; Vallée et al., 2017). Thus, it is unlikely to observe PEGS if the earthquake has low magnitude or if it ruptures slowly. For this reason, PEGS have only been identified for a handful of events (Vallée & Juhel, 2019). Though PEGS have shown strong potential to overcome the drawbacks of EEW systems, their extremely weak amplitudes (in the order of a few nanometers per second squared) have prevented operational applications. In this context, Licciardi et al. (2022) designed a deep convolutional neural network (CNN) called PEGSNet, to estimate earthquake location and to track the temporal evolution of the magnitude $M_w(t)$ of large earthquakes that can cause tsunamis in Japan, based solely on PEGS. The CNN is trained on a database made of synthetic PEGS waveforms plus real noise. Motivated by the success of PEGSNet in estimating the magnitude of the 2011 M_w 9.0 Tohoku-Oki earthquake in real time (Licciardi et al., 2022), we aim to export the algorithm to another tsunamigenic region, Chile, and evaluate the feasibility of proposing this method as a complementary tsunami early warning system. For this, we first re-train PEGSNet on the seismic network that recorded the 2010 M_w 8.8 Maule earthquake in order to assess its performance in rapidly estimating the magnitude of this mega-earthquake. We then re-train the algorithm on the seismic network presently available in order to assess how PEGSNet would perform currently for an earthquake in Chile.

2. Data

Given the limited number of PEGS observations, we create a synthetic database to train the CNN. We compute the theoretical waveforms at the location of the available stations generated by 500,000 sources with different locations, source time functions, seismic moments and focal mechanisms. The waveform computation uses a pre-constructed moment tensor database, which uses normal mode theory to build Green's functions between sources and receivers (Juhel et al., 2019). To make the synthetic signals realistic, we then add empirical noise (i.e., actual noise recorded at each station) to the modeled waveforms.

We use two seismic networks that were functional during 11 months in two different time periods: 2009–2010 and 2021–2022, referred to hereafter as the 2010 network and the 2021 network, respectively. The 2010 network is composed of 21 stations selected from those available through IRIS in Chile, Argentina and Brazil. These seismic stations recorded the 2010 Maule earthquake, allowing us to test PEGSNet on data from the earthquake. The
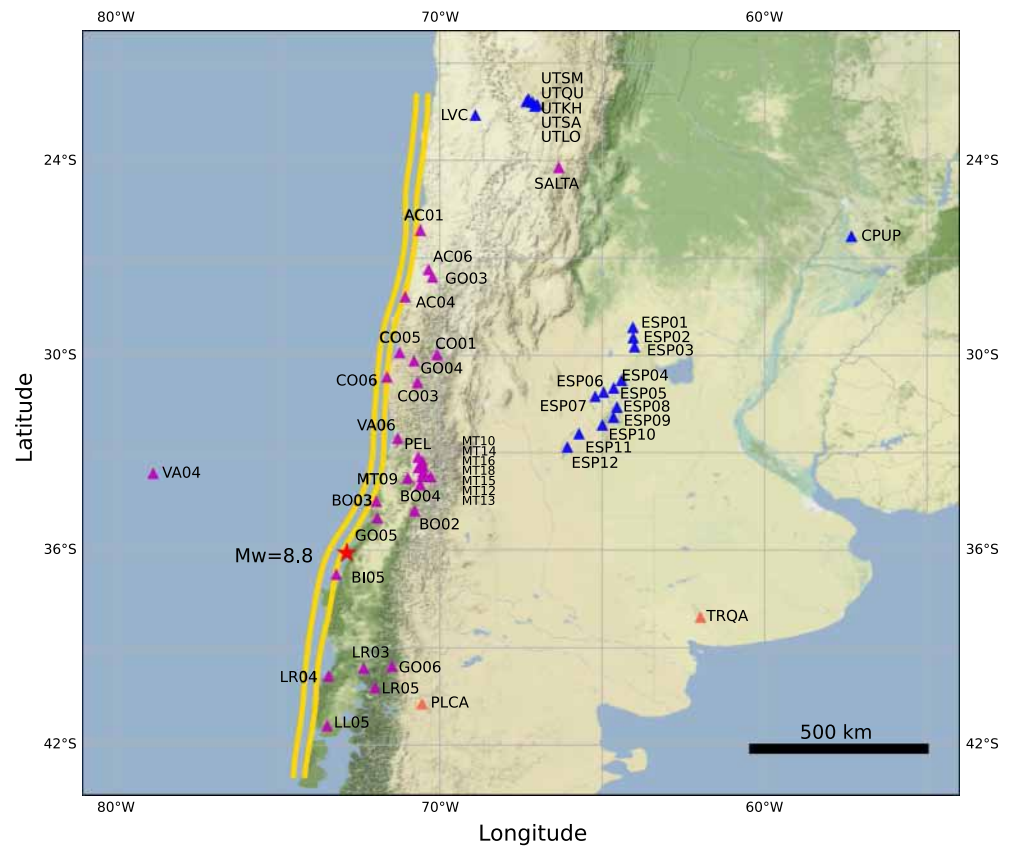
Figure 1. Two seismic networks and earthquake sources used in this work. The yellow dots indicate the location of the synthetic sources, they look like continuous lines because of their proximity. Blue triangles represent the stations of the 2010 network, purple triangles those of the 2021 network, and orange triangles the stations that belong to both networks. The red star represents the 2010 M_w 8.8 Maule earthquake epicenter.

2021 network contains 33 stations available via IRIS in Chile and Argentina. While there was no big earthquake between 2021 and 2022, we can evaluate on synthetic waveforms how PEGSNet would perform with the 2021 network configuration. The setup of the stations and synthetic sources is displayed in Figure 1.

For both networks, we select stations within a 2,000 km radius from all synthetic epicenters. According to Juhel et al. (2019), stations located in the P-wave extensional direction of the radiation pattern record strong gravity perturbation when deployed at distances between 1,000 and 2,000 km away from the epicenter of a large earthquake, due to the growing density anomaly generated by the rupture itself and the larger volume perturbed by the propagating seismic waves. At further distances, the perturbation decays, while at shorter distances the PEGS are rapidly hidden by the P-wave arrival.

2.1. Synthetics PEGS Database

We compute synthetic PEGS following the method of Juhel et al. (2019). It requires as inputs the earthquake centroid location, station locations, focal mechanism, Source Time Function (STF) and seismic moment (M_0). We consider 994 source locations, equally spaced along the 20 and 30 km iso-depths of the Chilean subduction megathrust, since all the earthquakes that caused tsunamis had centroids located in this depth range. The longitude, latitude, depth, strike and dip angles of all sources are consistent with the Slab2.0 model (Hayes et al., 2018). Rake angles for each source are drawn from a normal distribution with mean 90° and standard deviation 10°, and magnitudes from a uniform distribution between 6.0 and 10.0. Moment is calculated as $M_0 = 10^{1.5 M_w + 9.1}$ (in Newton-meters). We draw the STF from the empirical model proposed by Meier et al. (2017):

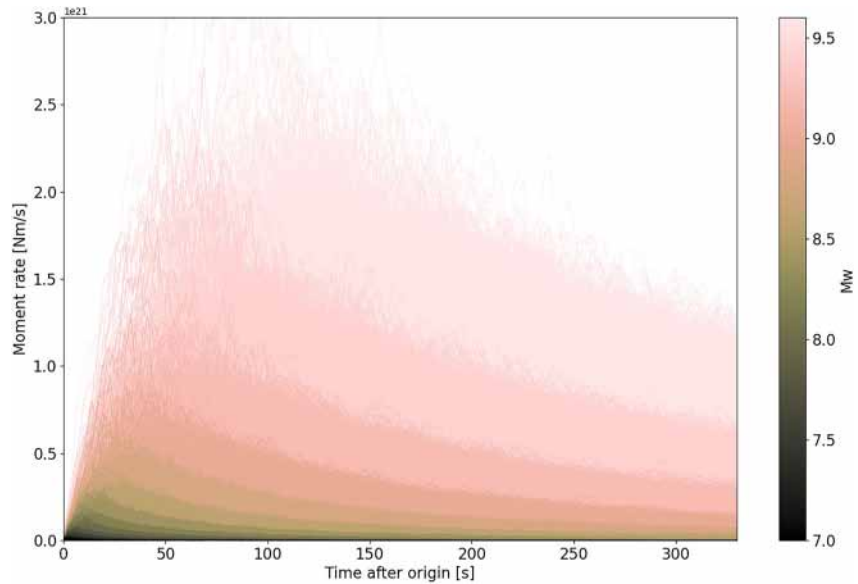$$STF(t) = M_0 \frac{f(t)}{\int f(t)\, dt},\qquad(2)$$

Figure 2. Source time functions used to generate the synthetic PEGS database, corresponding to magnitudes between 7.0 and 9.6.

where

$$f(t) = t \exp\left\{-0.5(\gamma t)^2\right\}[1 + N(t)], \tag{3a}$$

$$\gamma = 10^{7.24-0.41\log(M_0)+\epsilon}, \tag{3b}$$

$$N(t) = 0.38\frac{n(t)}{\sigma}, \tag{3c}$$

The random variable ϵ accounts for variability in the STF duration for a given M_0 and is drawn from a Gaussian distribution with zero mean and standard deviation of 0.15. The random component $N(t)$ models the fluctuations observed in real STFs. $n(t)$ is the time integral of a Gaussian noise time series with zero mean and standard deviation σ. Examples of STFs for different magnitudes are plotted in Figure 2.

The resulting synthetics are three-component (Z, N, and E) acceleration waveforms depicting the PEGS generated by earthquakes of large magnitude that might potentially occur in the Chilean subduction megathrust. They are sampled at 1 Hz and stored in windows of 700 s duration, centered at the origin time.

2.2. Empirical Noise Database

For both configurations, 2010 and 2021, the noise database is built from 11 months of continuous recordings, from May 2009 to April 2010 and from February 2021 to January 2022, respectively. The database is composed of 1-hr long traces that we pre-process as follows: instrumental response, mean and linear trend removal, and decimation to 1 Hz. We filter the recordings and synthetic waveforms as indicated in Vallée et al. (2017), using a 2.0 mHz high-pass, Butterworth, two poles, causal filter and a 30.0 mHz low-pass, Butterworth, six poles, causal filter.

From each 1-hr-long trace, we extract data windows of 700 s at randomly selected starting times. For one event, we use the same time interval for all stations to preserve spatial coherence of noise across the seismic network. We then add these noise samples to the synthetic PEGS and store each waveform as a 700 s long time series, centered on the earthquake origin time. We calculate the P-wave arrival time corresponding to each event-station pair in the synthetic waveform database, then set the signal to zero after that time and use the information of PEGS uniquely, to train the model. In a real-time scenario a P-phase picker would estimate the P-arrival time.

As in Licciardi et al. (2022), we clip traces at ± 10 nm/s^2 to eliminate high amplitudes and to limit the influence of high levels of noise. We scale amplitudes by 10 nm/s^2 to facilitate the convergence of the optimizer and to preserve information on the relative amplitudes of the PEGS. Additionally, we set to zero the amplitudes of the traces of 5% of the stations, randomly selected, for each event to simulate missing data and to limit over-fitting.
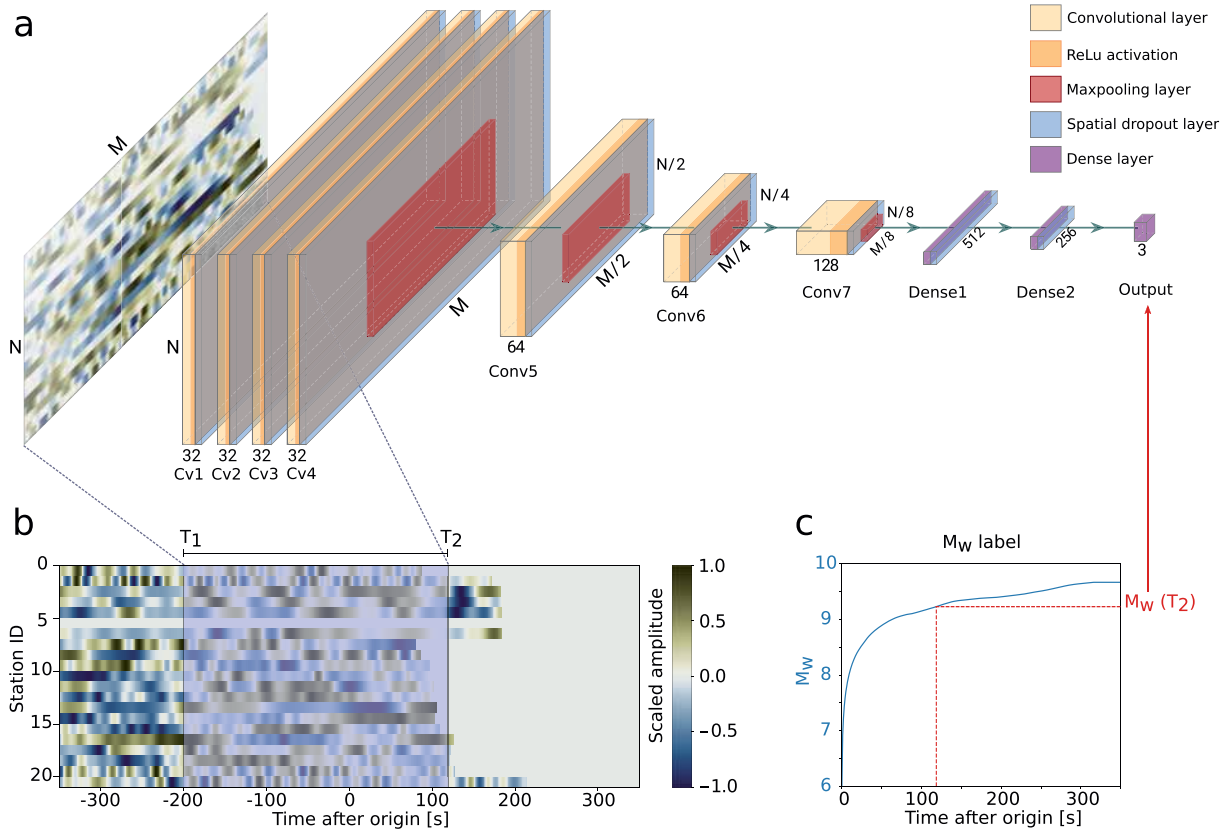
Figure 3. (a) PEGSNet architecture: The input data is a three-channel image (each channel corresponds to each component Z, N, and E), of shape $M \times N$, where M is the number of samples and N the number of seismic stations. (b) One example of the input data from the training database (vertical component only). The shaded area represents the input data for PEGSNet. The beginning of the input window T_1 is randomly selected and $T_2 = T_1 + 315$ s. (c) The blue line corresponds to the moment $M_w(t)$ for the selected event. The label assigned is $M_w(T_2)$ at the end of the window.

3. PEGSNet

3.1. Architecture

PEGSNet is a CNN that combines convolutional layers and fully connected layers in sequence (Figure 3), adopting a multi-station approach (Licciardi et al., 2022). We work with image-like inputs to train PEGSNet. Data are organized as images of size (M, N, c). M (=315) is the number of samples in 315 s long trace time windows, N is the number of stations and c (=3) is the number of components: vertical, east and north. The three outputs of the model are latitude (ϕ), longitude (λ) and moment magnitude ($M_w(t)$) at the time t of the last sample of the window.

The original architecture of PEGSNet designed by Licciardi et al. (2022) consists of eight convolutional blocks, but in this work, we use seven since the number of stations is less than that used in the cited work. Each block has one convolutional layer with rectified linear unit (ReLu) activation function and one dropout layer. Each convolutional layer has 32 filters from block 1 to block 4, 64 filters in blocks 5 and 6, 128 filters in block 7. Each convolutional layer uses a fixed kernel size of 3×3 and also a spatial dropout with a fixed rate of 4%. From block 4 we add maximum pooling layers to reduce the dimension of the input features by a factor of 4. This output is flattened and fed to a sequence of two dense layers of size 512 and 256, with a ReLu activation function and a spatial dropout with a rate of 4%. The output layer consists of three neurons that perform regression through a hyperbolic tangent activation function (Figure 3a). The number of parameters in the network is 1,535,139.

3.2. Training

The labeled ϕ and λ correspond to the true values used for the computation of the synthetic PEGS of each event. The labeled $M_w(t)$ is the moment magnitude used to calculate the synthetic PEGS at the time of the last waveform sample t. We extract the data of a running time window that starts at a randomly selected time t_1 and has a length
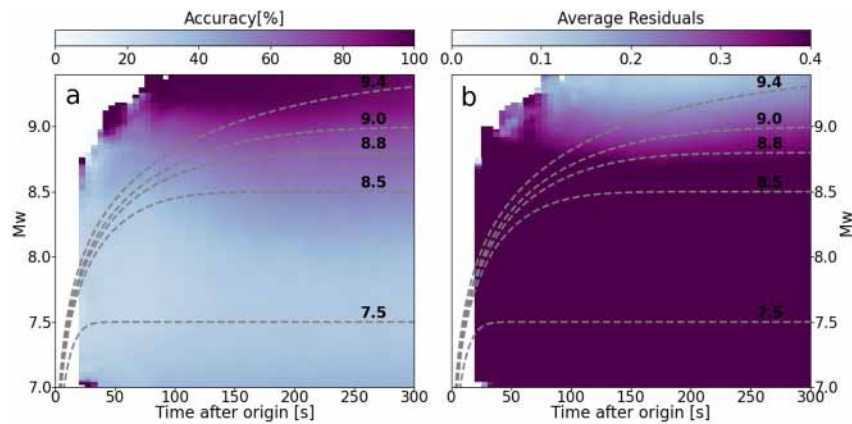
Figure 4. (a) Accuracy of the predictions on the test set as a function of time and magnitude. In each bin (pixel), the color represents the number of predictions whose distance to the ground truth is less than 0.4 magnitude units, divided by the total number of samples in the bin. The dashed lines represent the average values of the true $M_w(t)$ for events with the final magnitude indicated by the corresponding number. (b) Density map of the average residuals between the true and predicted magnitudes as a function of time and magnitude.

of 315 s. Then, we assign the value of $M_w(t_1 + 315 \text{ s})$ as the corresponding label (Figures 3b and 3c). In other words, PEGSNet is given a 315 s snapshot of the network's seismograms, and has to output the magnitude at the end of this snapshot.

The full database is divided into three parts: training, validation and test sets that comprise 80%, 10% and 10% of the database, respectively. The loss between the ground truth and the predicted values is minimized during training (200 epochs and batches of size 512) by measuring the mean absolute error. At the end of each epoch, the model is evaluated on the validation set. The model whose loss value is the lowest on the validation set is selected as the final model and is evaluated once again on the test set. PEGSNet has to be re-trained for each change in the network setup. We thus carried out the training twice: once on the 2010 network and once on the 2021 network. The corresponding training and validation curves can be found in Figure S1 in Supporting Information S1.

3.3. Testing

For each sample in the test set, a 315 s-long window $[t_1, t_2 = t_1 + 315 \text{ s}]$ slides through the data with a time step of 1 s. The starting window ends at the earthquake origin time t_0 ($t_2 = t_0$ and $t_1 = t_0 - 315 \text{ s}$) and the final window starts at the earthquake origin time ($t_2 = t_0 + 315 \text{ s}$ and $t_1 = t_0$). In between, PEGSNet reconstructs the STF by predicting $M_w(t_2)$ at each time step of 1 s.

4. PEGSNet Performance in Chile in 2010

4.1. Overall Performance

PEGSNet estimates the latitude ϕ and longitude λ of synthetic earthquakes, with errors on the order of 0.5° [55 km] for latitude and 0.2° [22 km] for longitude, after 120 s (see Figure S2 in Supporting Information S1). These results should not be over-interpreted since we implicitly provide the P-wave arrival times to PEGSNet by setting waveforms to 0 after the P arrival, making the location problem relatively trivial. We therefore mainly focus our analysis on the magnitude estimation.

We simulate a real-time scenario on each sample of the test set, by analyzing the data with a running time window of 315 s. Each window is fed to PEGSNet which estimates $M_w(t)$, the magnitude at the time of the last sample of the time window. Then, the window is shifted in steps of 1 s as PEGSNet progressively reconstructs the STF. We can evaluate how reliable the results are through accuracy maps (Figure 4). We define accuracy as the number of successful predictions divided by the total number of samples, with a prediction considered successful when its difference with the ground truth is less than 0.4 magnitude units. The maps in Figure 4 are calculated using all the samples of the test set. The outcome indicates that the model can track the moment released by earthquakes with magnitude equal to or higher than 8.8 with accuracy above 60% (Figure 4a) and errors below 0.37 (Figure 4b),
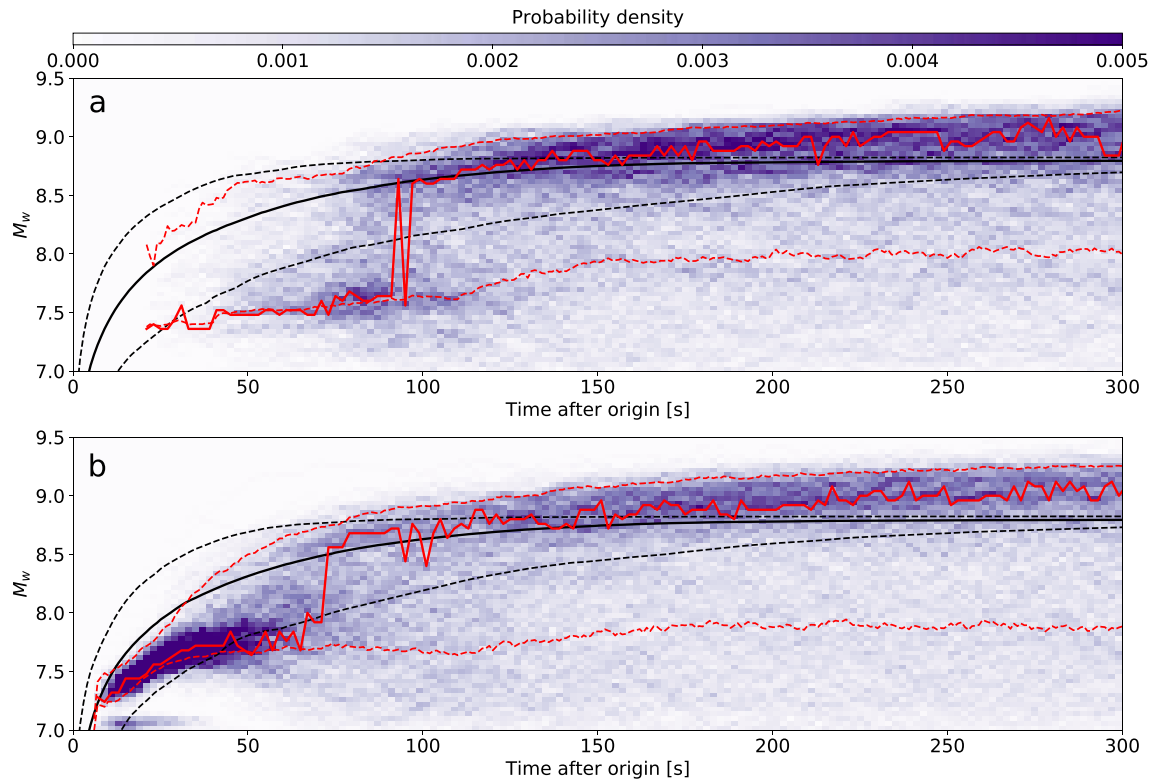
Figure 5. (a) Probability density of the magnitude estimation on M_w 8.8 synthetic earthquakes distributed everywhere along the Chilean subduction fault, with the 2010 network. The solid red line is the mode of the distribution. The red dashed lines limit the range between the 95 and 25 percentiles. The solid black line is the median of the ground truth, and the dashed black lines limit the range between the 95 and 5 percentiles. Panel (b) same as (a) for the 2021 network.

starting at 100 s after origin time. Earthquakes of magnitudes between 8.2 and 8.7 can be estimated with accuracy between 33% and 54% and errors above 0.42, 100 s after origin time.

4.2. Performance on M_w 8.8 Earthquakes

Testing the model with real earthquakes requires data recorded by the same stations used to train the model, or at least the majority of them. The stations available in 2010 were not the same as in posterior years because of the 21 stations that we used to train the model, 12 belonged to a temporary network (XH) that operated until August 2010. Therefore, we test PEGSNet's performance on M_w 8.8 synthetic earthquakes distributed everywhere along the Chilean subduction fault. Figure 5a shows the probability density of the magnitude estimation on the test set for all the predictions of events with final magnitude $M_w = 8.8 \pm 0.5$. Following the red solid line, which is the mode of the predictions, we see a clear underestimation of the magnitude before 100 s (when the true M_w is generally below 8.7 in our STF database) followed by a sudden jump after which the model starts tracking the evolution of the magnitude. This indicates that PEGSNet does not detect PEGS when the earthquake magnitude is below 8.7 and that estimations below that magnitude threshold should be interpreted as an absence of detected signal. Above this value, estimations start to be reliable, indicating the ongoing occurrence of a very large ($M_w \geq 8.7$), likely tsunamigenic, earthquake.

4.3. Playback of the Maule Earthquake

In order to validate the performance of PEGSNet, we use the actual Maule earthquake recordings. The processing of the raw data is the same as the one described in the Data section. We feed the model with the processed signals. The model outputs magnitude and location estimations every second starting at the origin time of the earthquake and using the previous 315 s of data, as described in the PEGSNet architecture section. Regarding the location estimations, we get mean errors of 0.33° [36 km] for latitudes and 0.28° [30 km] for longitudes (Figure S3 in Supporting Information S1). With respect to the magnitude estimations, we compare the results to the STF extracted from the SCARDEC database (Vallée & Douet, 2016) (Figure 6). We observe a clear underestimation
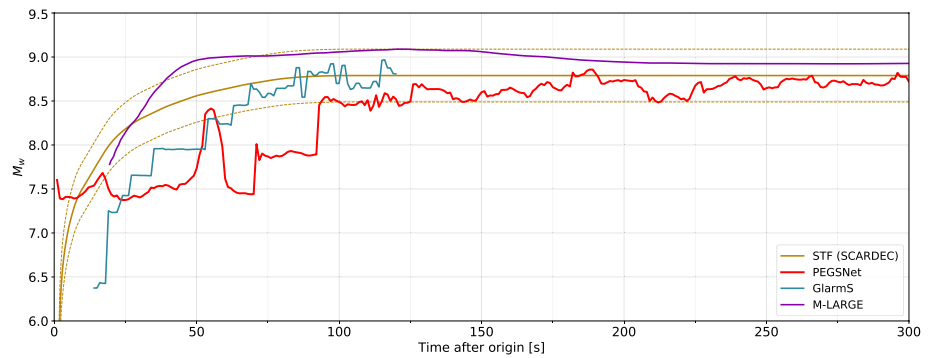
Figure 6. PEGSNet performance on real data for the Maule earthquake. The red curve shows the magnitude estimated by PEGSNet as a function of time using the recordings of the Maule earthquake. It is compared to the STF of the Maule earthquake in the SCARDEC database (Vallée & Douet, 2016) and to the estimations obtained by the G-larmS and M-LARGE algorithms. The golden dashed lines indicate ±0.3 magnitude units around the SCARDEC STF.

of the earthquake magnitude in the first 90 s. After 90 s, the model starts approaching the correct magnitude evolution.

We also compare our result to estimations obtained by other early warning algorithms such as G-larmS (C. J. Ruhl et al., 2019) and M-LARGE (Lin et al., 2021). The G-larmS estimation of the STF approaches the real STF before PEGSNet's (Figure 6). This belated stabilization is mainly due to the number of stations and distance to the sources. The model starts estimating the correct magnitude values once the P-wave has arrived at most stations (or at least a few seconds before when PEGS amplitude is the largest). The same model, trained with data recorded by a higher number of stations that are closer to the sources can give faster results, as seen in the Tohoku earthquake case (Licciardi et al., 2022) and in the 2021 network case (Section 5). G-larmS is coupled to the seismic point-source algorithm of ShakeAlert (C. Ruhl et al., 2017; C. J. Ruhl et al., 2019), which is an EEW system that uses a combination of the amplitude and frequency content of the first seconds of the P-wave arrival to estimate source parameters (C. Ruhl et al., 2017). Therefore, G-LarmS relies on prior constraints. M-LARGE is a deep learning model that characterizes earthquake magnitude in real time using data from more than 120 stations of the Chilean HR-GNSS network (Lin et al., 2021). M-LARGE takes 40 s to reach values within a range of 8.8 ± 0.3. However, at that time the earthquake is still ongoing and the final magnitude value is not yet reached (see the golden curve in Figure 6). For both G-larmS and M-LARGE, the results rely on using a priori assumptions on the slip distribution (McGuire et al., 2021) and are in contradiction with statistical analysis of earthquake source time functions (Meier et al., 2017). On the contrary, our approach requires no such a priori constraints and achieves similar theoretical performance only by leveraging signals traveling faster than seismic waves.

We perform four additional tests to assess the reliability of the model. In the first test, we generate synthetic PEGS using the SCARDEC STF of the Maule earthquake (Vallée & Douet, 2016) and add 1,000 different windows of noise recordings randomly taken from the test set. We then feed the model with these waveforms. The estimations indicate an accurate magnitude estimation starting a little after 100 s (Figure 7). The second test consists in feeding the model with the 1,000 windows of noise, to check that the estimations of M_w do not exceed 8.7, which is the sensitivity level of PEGSNet (Figure 8). The median of the magnitude estimations tends to remain constant at around 7.2, this value is considered the baseline corresponding to no PEGS detection. In the third test, we feed the model with one day of continuous records divided in 120 windows, in order to check if the algorithm will have false positives (magnitude estimation above the baseline of the model). This time, the sources are random so the P-arrival times are always different for each sample. The resulting magnitude values (see Figure S4a in Supporting Information S1) tend to have a similar behavior as the previous test but this time there is not such a sudden jump, even though it is clear that between 100 and 150 s the median starts approaching to the baseline. The last test consists in feeding the model with data containing four earthquakes of magnitudes between 4 and 5, with the same purpose as the third test. The respective estimations take values around and below the baseline (see Supplementary material Figure S4b in Supporting Information S1), except for one example (M_w 4.0) that takes high values at around 80 s and then decreases.
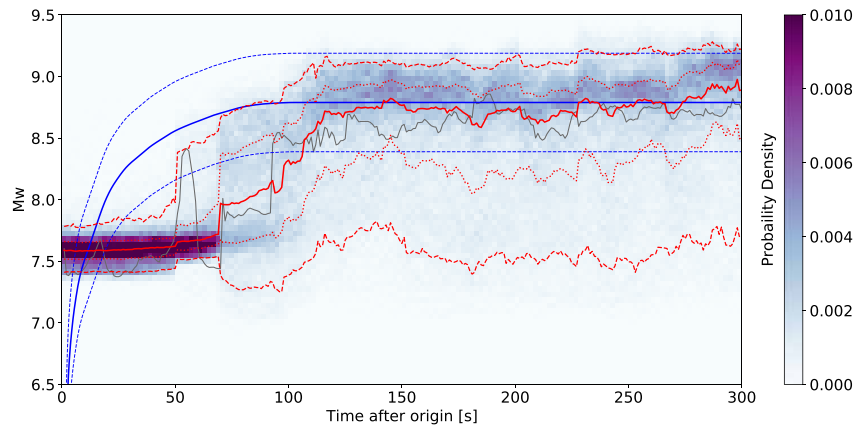
Figure 7. Density plot of PEGSNet magnitude estimations from 1,000 synthetic signals made of synthetic PEGS corresponding to the Maule earthquake source, augmented with 1,000 random noise time windows. The blue solid line represents the true STF taken from the SCARDEC database (Vallée & Douet, 2016), the same that we used to model the synthetics. The dashed blue lines indicate ±0.4 magnitude units around the SCARDEC STF. The red solid line is the median of the obtained distribution, the dotted red lines are the $Q1$–$Q3$ interquartile range and the dashed red lines limit the 5th and 95th percentiles. The gray solid line represents the magnitude estimated by PEGSNet using real data (same as in Figure 6).

5. PEGSNet Performance in Chile in 2021

5.1. Overall Performance

The results on the synthetic test set for the location, ϕ and λ, with the 2021 network are displayed in Supporting Information S1 (Figure S5). The estimations of latitudes have errors up to 0.37° (41 km) and the ones of longitudes present up to 0.1° (11 km), 90 s after the origin. These location results are better than with the 2010 network. This is because the estimations rely on the P-wave arrival times and the present network contains more stations closer to the earthquake source.

According to the accuracy calculations, PEGSNet on the 2021 network can track the moment released by earthquakes with magnitude equal to or higher than 8.8 with an accuracy above 55% (Figure 9a) and errors below 0.46 (Figures 9b), 100 s after the origin time. For earthquakes with magnitude between 8.2 and 8.7, the accuracy goes from 30% to 47% and errors between 0.5 and 0.75, after 100 s from the origin time. We select this time value in order to compare with the results obtained for the 2010 network, which are better than in the present configuration. The reason is that the 2021 network is mainly parallel and close to the sources, where the expected PEGS amplitudes of subduction earthquakes are minimal (Figure 10) (Vallée & Juhel, 2019). The leading contribution to the results is given by the only station located far from the trench, TRQA.
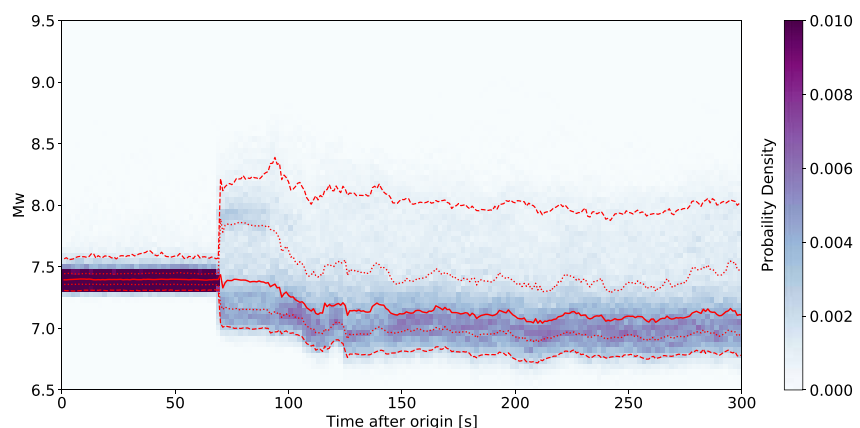

Figure 8. Magnitude estimations obtained by applying PEGSNet to noise: same as Figure 7 but removing the synthetic PEGS from the input data.
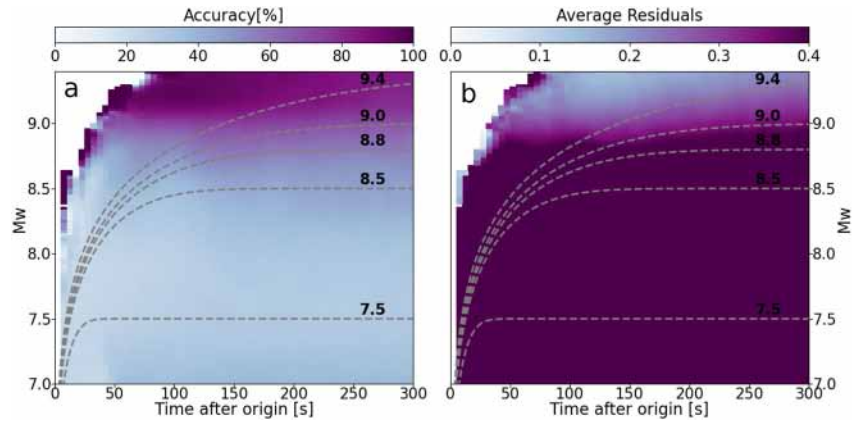
Figure 9. Same as Figure 4 for the 2021 network.

This highlights that PEGSNet performance is not only sensitive to the number of stations but also to their spatial distribution. According to the results obtained, PEGSNet's performance is more favorable with the contribution of stations located in the eastern part of the continent and far away from the sources, that is to say, in Argentina. For earthquakes comparable in magnitude to the Maule event, the ideal observation location for PEGS is ≈800 to 1,500 km west of the source (Figure 10). With potential sources distributed all along the Andean subduction
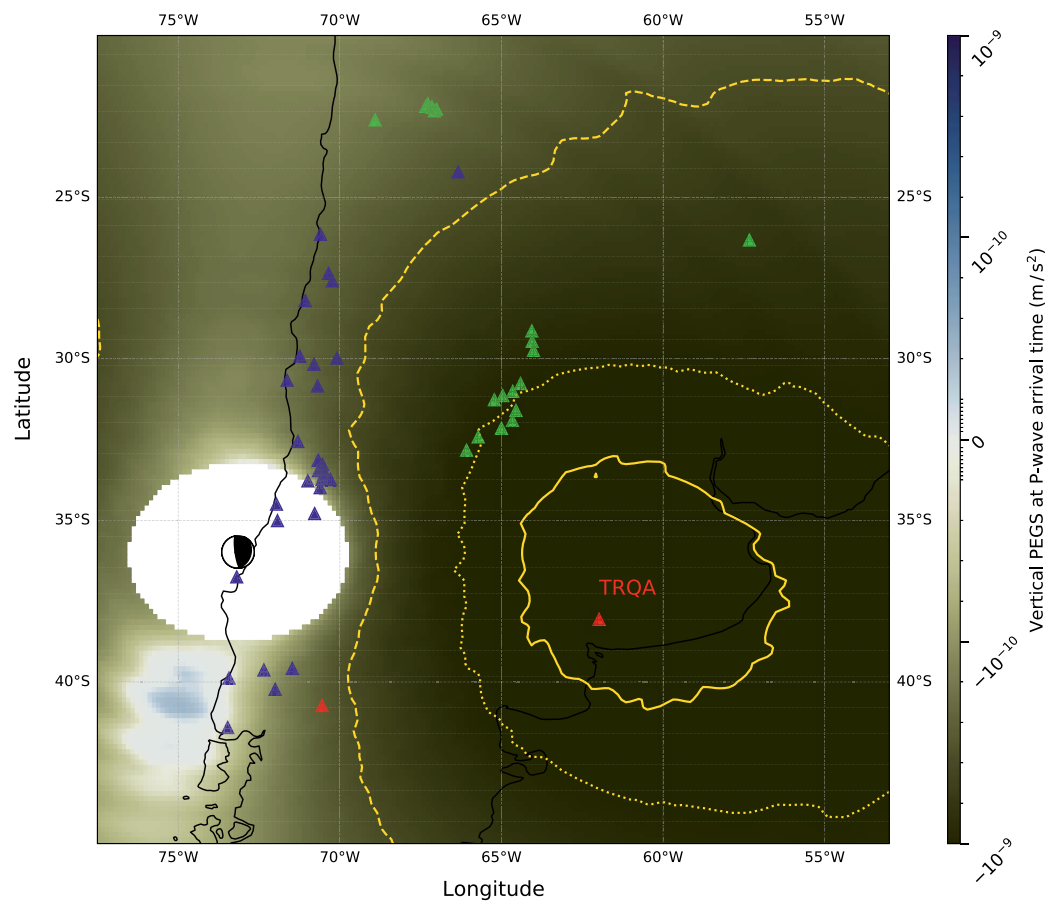

Figure 10. Spatial distribution of the maximum PEGS amplitude for the Maule earthquake, in the vertical component (at the P-wave arrival time). Green and blue triangles represent stations of the 2010 and 2021 networks, respectively. Red triangles are the stations common to the two networks. Solid contour lines are for ±1.3 nm/s², dotted for ±1.0 nm/s² and dashed for ±0.4 nm/s².
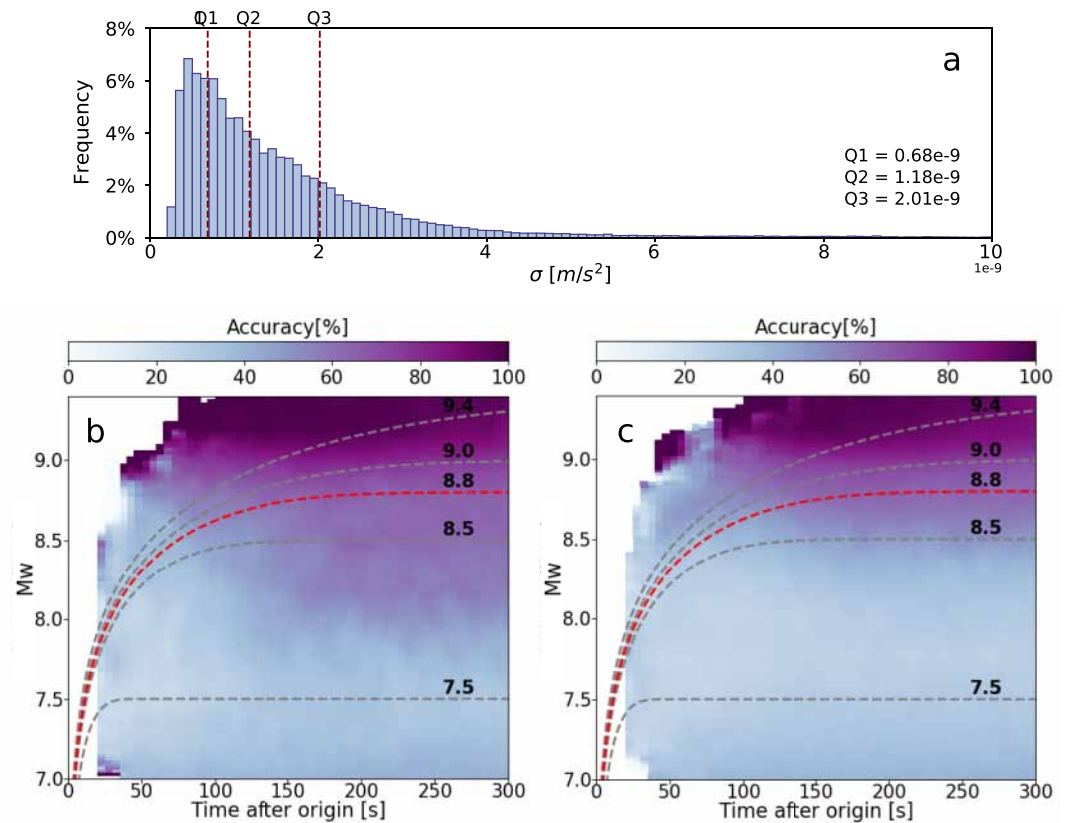
Figure 11. (a) Frequency distribution of the median standard deviation of the noise (σ) for the 2010 network test set, using a 5-min window previous to the event. The dashed red lines indicate the first ($Q1$), second ($Q2$) and third ($Q3$) quartiles. The bottom panels show the accuracy maps computed using the samples of the test set for which (b) $\sigma < Q1$ and (c) $\sigma > Q3$.

fault, as mentioned by Juhel et al. (2019), a geographical band can be defined where deploying stations could dramatically benefit PEGS-based tsunami warning systems. This zone should not be close to the coast as it is the 2021 network or the northernmost stations of the 2010 network.

5.2. Performance on M_w 8.8 Earthquakes

The probability density of the magnitude estimation on the test set for all the estimations of events with final magnitude $M_w = 8.8 \pm 0.5$ are shown in Figure 5b. Following the mode (red solid line), we see that we also underestimate the magnitude, but this time until 70 s approximately, followed by a jump after which the model starts tracking the evolution of the magnitude. This faster estimation compared to the 2010 case is because, in the 2021 scenario, there are more stations that are deployed close to the synthetic sources. This indicates that with the present seismic network, PEGSNet would output a faster magnitude estimation for a magnitude 8.8 event than with the seismic network available in 2010. However, for any earthquake, PEGSNet would perform with higher accuracy on the seismic network of 2010 than on the present one, as discussed in Sections 4.1 and 5.1.

6. Discussion

6.1. Noise Analysis

To evaluate the influence of the noise amplitude on PEGSNet's performance, we calculate the accuracy using different groups of samples of the test set, divided according to the noise level. We compute the standard deviation of a five-minute window of data before the P-wave arrival for each sample of the test set, and subsequently the median of the standard deviation over the whole seismic network. For both the 2010 and 2021 seismic networks, we then divide the test sets into four subsets defined by the three quartiles of the distribution: $Q1$, $Q2$,
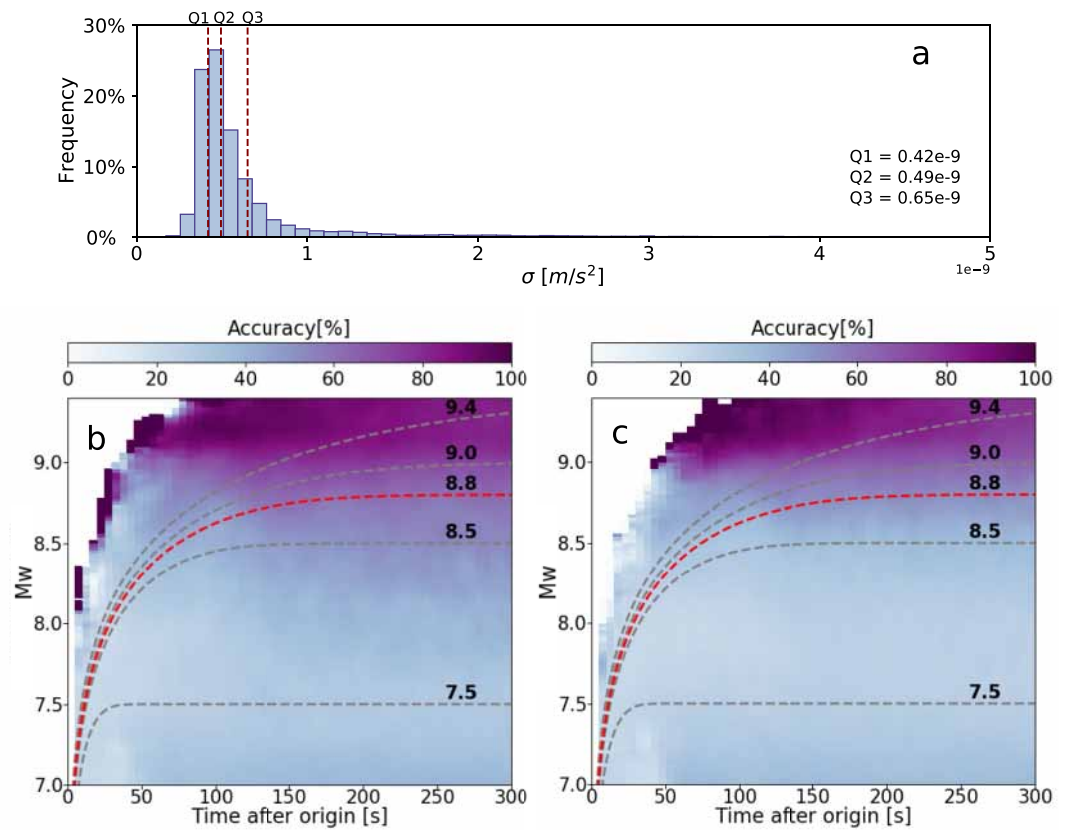
Figure 12. Same as Figure 11 for the 2021 network.

and $Q3$. The values of the three quartiles are displayed in Figures 11a and 12a for the 2010 and 2021 networks, respectively. In both cases, the accuracy of the estimations decreases when the level of noise increases. This is summarized in Table 1, where the accuracy values have been calculated for the events with magnitude equal to or higher than 8.8, after 100 s of the origin time. Even though the level of noise of the 2010 network is higher than the one of the 2021 network, the accuracy of the estimations is better. These results come from the fact that 2010 network contains stations where the amplitudes of PEGS are large, while 2021 network stations are very close to the sources and the amplitudes of PEGS are small (Figure 10). Thus, in our case study, the spatial configuration of the seismic network is more important than the number of stations and even than its level of noise.

6.2. Test on Noiseless Data

To explore the theoretical limits of PEGSNet and find an upper limit in the performance, we train and test the model considering an idealized scenario of noiseless data. We use the synthetic PEGS database described previously, but do not add noise. The density plot of the residuals in Figure 14 shows again the evident difference in the timeliness of the estimations between the two networks: the 2021 network provides earlier estimates than the 2010 network. The estimations based on the 2010 network start at around 20 s and have errors of ± 0.2 after the first 50 s (Figure 14a). The estimations based on the 2021 network start within 10 s after origin time and have errors of ± 0.2 but with higher dispersion up to around 60 s. According to the corresponding accuracy maps (Figure 13), the first estimates start earlier with the 2021 network but the accuracy is also poorer than with the 2010 network, as discussed in Sections 4 and 5.

Table 1
Values of the Noise Analysis

σ	2010 network		2021 network	
	Accuracy	Misfit	Accuracy	Misfit
$<Q1$	62%	0.35	59%	0.39
$>Q3$	59%	0.43	51%	0.59

Note. Accuracy and misfit values calculated using the $M_w \geq 8.8$ earthquakes 100 s after the origin time and that belong to the first and fourth subset of the test set, for the 2010 and 2021 networks. The first subset (lowest level of noise) contains the samples for which $\sigma < Q1$. The fourth subset (higher level of noise) contains the samples for which $\sigma > Q3$. Q1 and Q3 values are indicated in panel (a) of Figures 11 and 12
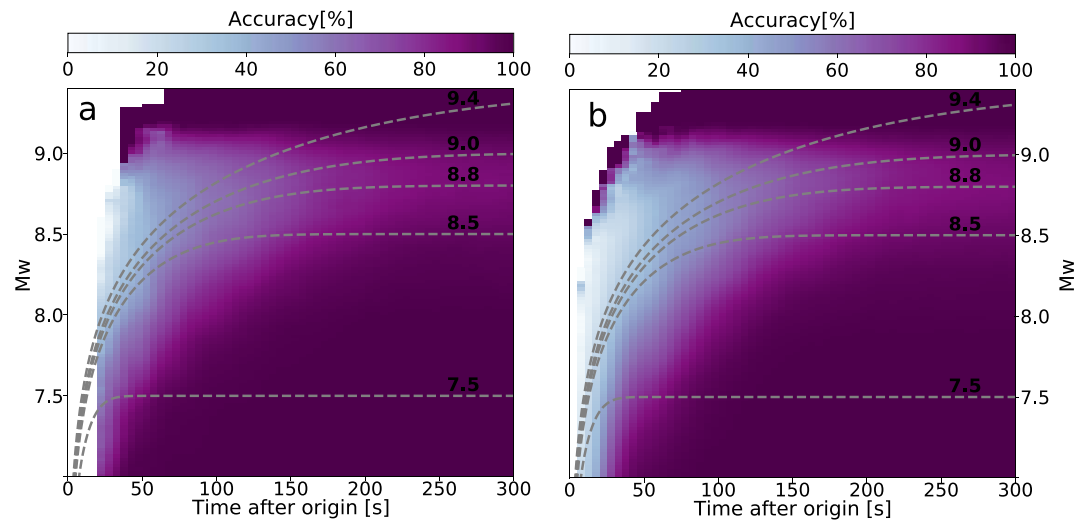
Figure 13. Accuracy map using the noise-free PEGS database, test set only. Panels (a) and (b) correspond to 2010 and 2021 networks, respectively.

7. Conclusion

We trained PEGSNet, a Convolutional Neural Network that estimates the evolution of an earthquake's source time function based on Prompt Elasto-Gravity Signals, with data recorded by the seismic networks available in Chile in 2010 and 2021. The former contains fewer stations and noisier data. Our study confirms that PEGS can be used for rapid estimation of the magnitude of large earthquakes, with performance competitive with GNSS-based algorithms for the 2010 M_w 8.8 Maule earthquake, but without requiring a priori assumptions on slip distribution. This supports the potential implementation of the method as a complement to tsunami warning systems. Regarding the results for different setups, the model shows delayed estimations of moment release, but higher accuracy values when using the 2010 configuration. The 2021 network provides estimations sooner owing to its higher number of stations and their proximity to the subduction sources. Nevertheless, this latter aspect played an adverse role in
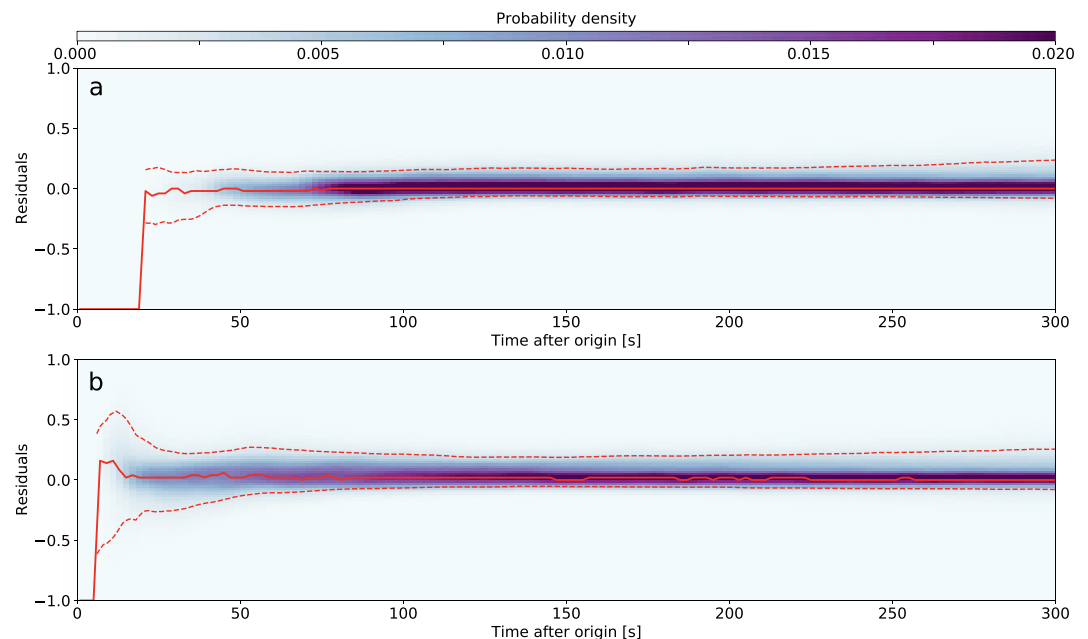

Figure 14. Density plot of the residuals between the predicted magnitude and the ground truth as a function of time for the test set of the noise-free PEGS database. Panels (a) and (b) correspond to the results using the 2010 and 2021 networks, respectively.

the model performance because the closer stations do not record the PEGS with the largest amplitudes, meaning that PEGSNet is more sensitive to the geometry of the network than to the number of stations. This would limit applications to operational early warning as a stand alone system. However, the performance on Maule attests that PEGSnet could be of use as a complementary algorithm for tsunami warning that could bring additional and more reliable information when the magnitudes reaches values over 8.7. The aspects covered herein, give us a better outlook on the requirements for improving the performance of PEGS-based early warning approaches, such as the deployment of seismic stations where the larger amplitudes of PEGS are expected. In this particular study case, in locations parallel to the trench and simultaneously at more than 800 km inland.

Data Availability Statement

The facilities of IRIS Data Services were used for access to waveform and metadata from IRISDMC (network code: C, C1, G, GT, IU, XH, and YS) and GEOFON (network code GE) datacenters. PEGSNet, the CNN used in this work was developed by Licciardi et al. (2022). Figures were made with Matplotlib version 3.3.4.

References

Allen, R. M., & Kanamori, H. (2003). The potential for earthquake early warning in southern California. *Science*, *300*(5620), 786–789. https://doi.org/10.1126/science.1080912

Allen, R. M., & Melgar, D. (2019). Earthquake early warning: Advances, scientific challenges, and societal needs. *Annual Review of Earth and Planetary Sciences*, *47*(1), 361–388. https://doi.org/10.1146/annurev-earth-053018-060457

Bock, Y., & Melgar, D. (2016). Physical applications of GPS geodesy: A review. *Reports on Progress in Physics*, *79*(10), 106801. https://doi.org/10.1088/0034-4885/79/10/106801

Boore, D., & Bommer, J. (2005). Processing of strong-motion accelerograms: Needs, options and consequences. *Soil Dynamics and Earthquake Engineering*, *25*(2), 93–115. https://doi.org/10.1016/j.soildyn.2004.10.007

Harms, J. (2016). Transient gravity perturbations from a double-couple in a homogeneous half-space. *Geophysical Journal International*, *205*(2), 1153–1164. https://doi.org/10.1093/gji/ggw076

Harms, J., Ampuero, J.-P., Barsuglia, M., Chassande-Mottin, E., Montagner, J.-P., Somala, S., & Whiting, B. (2015). Transient gravity perturbations induced by earthquake rupture. *Geophysical Journal International*, *201*(3), 1416–1425. https://doi.org/10.1093/gji/ggv090

Hayes, G., Moore, G., Portner, D., Hearne, M., Flamme, H., Furtney, M., & Smoczyk, G. (2018). Slab2, a comprehensive subduction zone geometry model. *Science*, *362*(6410), 58–61. https://doi.org/10.1126/science.aat4723

Heaton, T. H. (2017). Correspondence: Response of a gravimeter to an instantaneous step in gravity. *Nature Communications*, *8*(1), 1–3. https://doi.org/10.1038/s41467-017-01348-z

Hoshiba, M., Iwakiri, K., Hayashimoto, N., Shimoyama, T., Hirano, K., Yamada, Y., et al. (2011). Outline of the 2011 off the pacific coast of Tohoku earthquake (M_w 9.0) — Earthquake early warning and observed seismic intensity. *Earth Planets and Space*, *63*(7), 547–551. https://doi.org/10.5047/eps.2011.05.031

Hoshiba, M., & Ozaki, T. (2014). Earthquake early warning and tsunami warning of the Japan meteorological agency, and their performance in the 2011 off the pacific coast of Tohoku earthquake (M_w9.0). In F. Wenzel & J. Zschau (Eds.), *Early warning for geological disasters: Scientific methods and current practice* (pp. 1–28). Springer Berlin Heidelberg. https://doi.org/10.1007/978-3-642-12233-0_1

Juhel, K., Ampuero, J.-P., Barsuglia, M., Bernard, P., Chassande-Mottin, E., Fiorucci, D., et al. (2018). Earthquake early warning using future generation gravity strainmeters. *Journal of Geophysical Research: Solid Earth*, *123*(12), 10–889. https://doi.org/10.1029/2018jb016698

Juhel, K., Montagner, J.-P., Vallée, M., Ampuero, J.-P., Barsuglia, M., Bernard, P., et al. (2019). Normal mode simulation of prompt elastogravity signals induced by an earthquake rupture. *Geophysical Journal International*, *216*(2), 935–947. https://doi.org/10.1093/gji/ggy436

Licciardi, A., Bletery, Q., Rouet-Leduc, B., Ampuero, J.-P., & Juhel, K. (2022). Instantaneous tracking of earthquake growth with elastogravity signals. *Nature*, *606*(7913), 319–324. https://doi.org/10.1038/s41586-022-04672-7

Lin, J.-T., Melgar, D., Thomas, A., & Searcy, J. (2021). Early warning for great earthquakes from characterization of crustal deformation patterns with deep learning. *Journal of Geophysical Research: Solid Earth*, *126*(10), e2021JB022703. https://doi.org/10.1029/2021jb022703

McGuire, J., Minson, S., Murray, J., & Brooks, B. (2021). The role of geodetic algorithms for earthquake early warning in Cascadia. *Geophysical Research Letters*, *48*(6), e2020GL092324. https://doi.org/10.1029/2020GL092324

Meier, M.-A., Ampuero, J. P., & Heaton, T. H. (2017). The hidden simplicity of subduction megathrust earthquakes. *Science*, *357*(6357), 1277–1281. https://doi.org/10.1126/science.aan5643

Meier, M.-A., Heaton, T., & Clinton, J. (2016). Evidence for universal earthquake rupture initiation behavior. *Geophysical Research Letters*, *43*(15), 7991–7996. https://doi.org/10.1002/2016GL070081

Melgar, D., Allen, R. M., Riquelme, S., Geng, J., Bravo, F., Baez, J. C., et al. (2016). Local tsunami warnings: Perspectives from recent large events. *Geophysical Research Letters*, *43*(3), 1109–1117. https://doi.org/10.1002/2015GL067100

Melgar, D., & Bock, Y. (2013). Near-field tsunami models with rapid earthquake source inversions from land- and ocean-based observations: The potential for forecast and warning. *Journal of Geophysical Research: Solid Earth*, *118*(11), 5939–5955. https://doi.org/10.1002/2013JB010506

Minson, S. E., Meier, M.-A., Baltay, A. S., Hanks, T. C., & Cochran, E. S. (2018). The limits of earthquake early warning: Timeliness of ground motion estimates. *Science Advances*, *4*(3), eaaq0504. https://doi.org/10.1126/sciadv.aaq0504

Minson, S. E., Murray, J. R., Langbein, J. O., & Gomberg, J. S. (2014). Real-time inversions for finite fault slip models and rupture geometry based on high-rate GPS data. *Journal of Geophysical Research: Solid Earth*, *119*(4), 3201–3231. https://doi.org/10.1002/2013jb010622

Montagner, J.-P., Juhel, K., Barsuglia, M., Ampuero, J. P., Chassande-Mottin, E., Harms, J., et al. (2016). Prompt gravity signal induced by the 2011 Tohoku-Oki earthquake. *Nature Communications*, *7*(1), 1–7. https://doi.org/10.1038/ncomms13349

Ruhl, C., Melgar, D., Grapenthin, R., & Allen, R. M. (2017). The value of real-time GNSS to earthquake early warning. *Geophysical Research Letters*, *44*(16), 8311–8319. https://doi.org/10.1002/2017GL074502

Ruhl, C. J., Melgar, D., Chung, A. I., Grapenthin, R., & Allen, R. M. (2019). Quantifying the value of real-time geodetic constraints for earthquake early warning global seismic and geodetic data set. *Journal of Geophysical Research: Solid Earth*, *124*(4), 3819–3837. https://doi.org/10.1029/2018jb016935

Setiyono, U., Gusman, A. R., Satake, K., & Fujii, Y. (2017). Pre-computed tsunami inundation database and forecast simulation in Pelabuhan Ratu, Indonesia. *Pure and Applied Geophysics*, *174*(8), 3219–3235. https://doi.org/10.1007/s00024-017-1633-8

Shimoda, T., Juhel, K., Ampuero, J.-P., Montagner, J.-P., & Barsuglia, M. (2021). Early earthquake detection capabilities of different types of future-generation gravity gradiometers. *Geophysical Journal International*, *224*(1), 533–542. https://doi.org/10.1093/gji/ggaa486

Vallée, M., Ampuero, J.-P., Juhel, K., Bernard, P., Montagner, J.-P., & Barsuglia, M. (2017). Observations and modeling of the elastogravity signals preceding direct seismic waves. *Science*, *358*(6367), 1164–1168. https://doi.org/10.1126/science.aao0746

Vallée, M., & Douet, V. (2016). A new database of source time functions (STFs) extracted from the SCARDEC method. *Physics of the Earth and Planetary Interiors*, *257*, 149–157. https://doi.org/10.1016/j.pepi.2016.05.012

Vallée, M., & Juhel, K. (2019). Multiple observations of the prompt elastogravity signals heralding direct seismic waves. *Journal of Geophysical Research: Solid Earth*, *124*(3), 2970–2989. https://doi.org/10.1029/2018jb017130

Wu, Y.-M., & Zhao, L. (2006). Magnitude estimation using the first three seconds p-wave amplitude in earthquake early warning. *Geophysical Research Letters*, *33*(16), L16312. https://doi.org/10.1029/2006GL026871

Zhang, S., Wang, R., & Chen, X. (2022). Seismic prompt gravity strain signals in a layered spherical Earth. SSRN 4245177 Retrieved from https://ssrn.com/abstract=4245177

Zhang, S., Wang, R., Dahm, T., Zhou, S., & Heimann, S. (2020). Prompt elasto-gravity signals (PEGS) and their potential use in modern seismology. *Earth and Planetary Science Letters*, *536*, 116150. https://doi.org/10.1016/j.epsl.2020.116150